electronics

MDPI

Article

Triple-Band Terahertz Chiral Metasurface for Spin-Selective Absorption and Reflection Phase Manipulation

Hang Zhang [1,2], Liming Si [1,2,*], Tianyu Ma [1], Lin Dong [1], Rong Niu [1], Xiue Bao [1], Houjun Sun [1] and Jun Ding [3]

[1] Beijing Key Laboratory of Millimeter Wave and Terahertz Technology, School of Integrated Circuits and Electronics, Beijing Institute of Technology, Beijing 100081, China
[2] Yangtze Delta Region Academy, Beijing Institute of Technology, Jiaxing 314019, China
[3] State Key Laboratory of Precision Spectroscopy, Key Laboratory of Polar Materials and Devices, School of Physics and Electronic Sciences, East China Normal University, Shanghai 200241, China
* Correspondence: lms@bit.edu.cn

Abstract: In this paper, a triple-band terahertz chiral metasurface is proposed, which could realize spin-selective absorption (SSA) effect and efficient independent phase manipulation in three distinct frequency bands. Through the simulation of the surface current distribution, we explain the mechanism of the triple-band SSA effect. Furthermore, the introduction of Pancharatnam–Berry phase endows the metasurface with the ability to manipulate the reflection phase at the chiral resonance frequencies, which enabled simultaneous amplitude and phase manipulation of CP waves through different phase coding strategies. To test this concept, two terahertz SSA-coding metasurfaces were designed and simulated, which have the function of four-beam splitting and vortex wave anomalous reflection, respectively. These simple-structured multifunctional devices demonstrate the application prospects of the metasurface in terahertz chiral sensing, imaging, secure communications, etc.

Keywords: terahertz; chiral metasurface; coding metasurface; circular dichroism; Pancharatnam–Berry phase

check for updates

Citation: Zhang, H.; Si, L.; Ma, T.; Dong, L.; Niu, R.; Bao, X.; Sun, H.; Ding, J. Triple-Band Terahertz Chiral Metasurface for Spin-Selective Absorption and Reflection Phase Manipulation. *Electronics* **2022**, *11*, 4195. https://doi.org/10.3390/electronics11244195

Academic Editor: Paolo Baccarelli

Received: 28 November 2022
Accepted: 14 December 2022
Published: 15 December 2022

1. Introduction

Terahertz waves refer to electromagnetic waves with frequencies in the range of 0.1 to 10 THz, which have great application potential in the fields of sixth-generation (6G) mobile communications, security monitoring, non-destructive testing, and space situational awareness [1]. Since it is difficult for natural materials to generate effective terahertz responses, the development of terahertz functional devices is limited, forming a "Terahertz Gap" in the electromagnetic spectrum [2]. Metasurfaces are the planar counterpart of metamaterials, which have been proven to have unique electromagnetic wave control capabilities [3]. At present, many metasurfaces that possess various functionalities have been proposed, such as wave absorption [4,5], metalens focusing [6,7], asymmetric transmission [8–10], polarization conversion [11,12], and vortex beam generation [13,14]. In the field of terahertz and quantum nanophotonics research, impressive progress has been made in recently reported metasurface devices, such as full-stokes polarization perfect absorbers realized by diatomic plasmonic metasurfaces [15], dark-mode absorbers for studying optical bound states in the continuum [16], terahertz plasmonic absorbers for biological detection and biochemical sensing applications [17], etc. These advances and related applications demonstrate that terahertz devices based on metasurface design could be a powerful method to solve the terahertz technology bottleneck.

Although most of the reported metasurfaces are designed to manipulate the linearly polarized (LP) waves, the control of circularly polarized (CP) waves requires the use of chiral metasurfaces. Chirality is a geometric property that lacks any mirror symmetry plane, and is widely present in structures such as DNA molecules and proteins [18]. Since

chiral structures can respond differently to left-handed circularly polarized (LCP) and right-handed circularly polarized (RCP) waves, terahertz chiral metasurfaces have attracted great attention in spin photonics. Among them, chiral metasurfaces with the spin-selective absorption (SSA) effect have attracted a lot of attention, which can absorb a single spin state of the CP waves while reflecting the orthogonal one. This differential absorption capability of the chiral metasurfaces can be measured by the circular dichroism (CD) index [19]. Utilizing chiral metasurfaces to generate giant CD and manipulate CP waves is critical for numerous applications, including chiral imaging [20], CP light detection [21], and chiral biomolecule analysis [22].

In the past few years, a variety of SSA chiral metasurfaces have been reported in frequencies ranging from microwave to optics [23–38]. In addition, the dynamic manipulation of the terahertz CD is further realized by introducing materials such as vanadium dioxide or graphene [27–30]. In order to achieve multi-dimensional manipulation of the CP waves while maintaining the CD effect, the Pancharatnam–Berry (PB) phase has been introduced into the chiral metasurfaces to achieve functions such as anomalous reflection [31,32], vortex beam generation [33], and terahertz chiral imaging [34]. However, most of these chiral metasurfaces for CP waves amplitude and phase modulation can only function at a single frequency point. Although some dual-band chiral metasurfaces with CD have been reported [35–38], the design schemes lack the space to further extend the operation frequency bands, and many designs cannot independently manipulate the wavefront of the CP waves in corresponding frequency bands. As a result, it is still challenging to find a design method for chiral metasurfaces that can simultaneously manipulate the amplitude and phase of the CP waves in multiple bands.

In this work, we proposed a chiral metasurface that can independently modulate the reflection amplitude and phase responses of the CP waves in three distinct frequency bands. In order to generate strong chiral resonances in the metallic resonant ring, the metasurface was designed according to a general design principle of symmetry breaking. The simulation results showed that the chiral metasurface attained the CD summits of 0.8, −0.66, and 0.64 at 1 THz, 1.17 THz, and 1.29 THz, respectively. In addition, the working mechanism of the triple-band SSA effect were investigated and explained. Meanwhile, we achieved the whole 2π reflection PB phase coverage. Therefore, the SSA effect and reflection phase manipulation could be fulfilled simultaneously with this metasurface by using different coding strategies. As a verification, two types of triple-band terahertz spin-selective devices were investigated, which function as a four-beam splitter and a vortex beam generator with an anomalous reflection angle, respectively. Traditionally, these spin-selective multifunction devices can only be realized by cascading linear polarizers, wave plates, and absorbers, which often leads to a bulky size. Thus, this chiral metasurface with a simple structure and easy integration could have distinctive applications in terahertz secure communication, chiral sensing, and chiral biomedical detection and imaging.

2. Models and Theories

According to the deduction of a Jones matrix for the reflection characteristics of the metasurface, this type of metasurface unit cells with SSA effect should break n-fold ($n > 2$) and mirror symmetries simultaneously [23]. To meet this special structural symmetry requirement, we construct a triple-band SSA asymmetric split-ring resonator (T-SRR) as the basic unit pattern, which consists of four chiral metal strips placed symmetrically along the center of the top surface of the dielectric plate, as shown in Figure 1a. These four chiral metal structures are all made of gold with a conductivity of $\sigma = 4.56e7$ S/m, and the dimension parameters and values are shown in Table 1. This unit cell has a period of 100 μm, and the top metal pattern, dielectric substrate, and bottom metal shield form the three-layer structure of the unit cell. We chose polydimethylsiloxane (PDMS) as the dielectric substrate with a relative permittivity of 2.35 and loss tangent of 0.025. The thickness of the dielectric substrate is 33 μm while the metal on the top pattern and bottom ground shield is 200 nm. Figure 1b shows the schematic diagram of the triple-band SSA effect of the T-SRR unit cell.

Specifically, the T-SRR can absorb the incident LCP waves at 1 and 1.29 THz, and reflect the incident RCP waves with suppression of the handedness change, while absorbing the incident RCP waves at 1.17 THz, and reflecting the incident LCP waves with suppression of the handedness change. In summary, the T-SRR could achieve a triple-band CD.

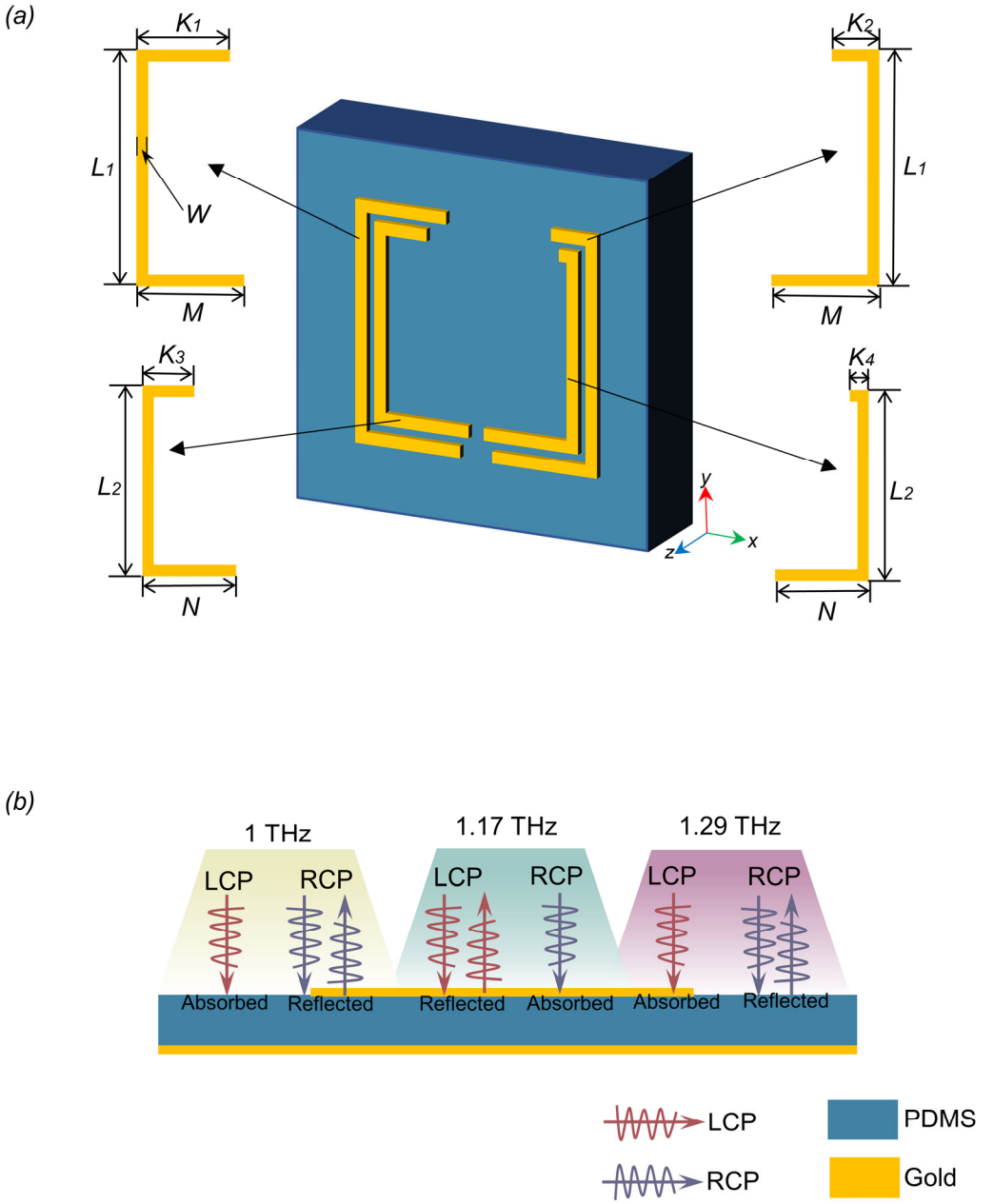

Figure 1. (**a**) Model and structural parameters of the T-SRR unit cell and the four kinds of chiral metal strips; (**b**) Functional diagram of the T-SRR unit cell.

Table 1. The dimension parameters of the T-SRR metal structures.

Parameter Name	L_1	L_2	K_1	K_2	K_3	K_4	M	N	W
Value	66	55	26	13.2	15	5.5	30	27	3.3

Unit: μm.

As the bottom metal ground shields the transmission of incident waves, only the reflection field needs to be considered when analyzing the performance of the SSA. In

the Cartesian coordinate system, the relationship between the incident electric field and reflected electric field under the LP incidence can be expressed as:

$$\begin{pmatrix} \boldsymbol{E}_{\mathrm{R}}^{x} \\ \boldsymbol{E}_{\mathrm{R}}^{y} \end{pmatrix} = \begin{pmatrix} r_{xx} & r_{xy} \\ r_{yx} & r_{yy} \end{pmatrix} \begin{pmatrix} \boldsymbol{E}_{\mathrm{I}}^{x} \\ \boldsymbol{E}_{\mathrm{I}}^{y} \end{pmatrix} = \boldsymbol{R} \begin{pmatrix} \boldsymbol{E}_{\mathrm{I}}^{x} \\ \boldsymbol{E}_{\mathrm{I}}^{y} \end{pmatrix} \tag{1}$$

where $\boldsymbol{E}_{\mathrm{R}}$ and $\boldsymbol{E}_{\mathrm{I}}$ represent the reflected electric field and the incident electric field, respectively; r represents the reflection coefficient, "x" and "y" represent the linear polarization directions; and $\boldsymbol{R}$ is the reflection matrix. By the matrix transformation, the LP basis reflection matrix $\boldsymbol{R}$ could be transformed into the CP basis reflection matrix $\boldsymbol{R}_{\mathrm{circ}}$:

$$\boldsymbol{R}_{\mathrm{circ}} = \begin{pmatrix} r_{LR} & r_{LL} \\ r_{RR} & r_{RL} \end{pmatrix} = \boldsymbol{\Lambda}^{-1}\boldsymbol{R}\boldsymbol{\Lambda} = \frac{1}{2}\begin{pmatrix} r_{xx} + r_{yy} + \mathrm{i}(r_{xy} - r_{yx}) & r_{xx} - r_{yy} - \mathrm{i}(r_{xy} + r_{yx}) \\ r_{xx} - r_{yy} + \mathrm{i}(r_{xy} + r_{yx}) & r_{xx} + r_{yy} - \mathrm{i}(r_{xy} - r_{yx}) \end{pmatrix} \tag{2}$$

The transformation matrix $\boldsymbol{\Lambda} = \frac{1}{\sqrt{2}}\begin{pmatrix} 1 & 1 \\ \mathrm{i} & -\mathrm{i} \end{pmatrix}$, r_{LL}, and r_{RR} are co-polarized reflection coefficients; r_{LR} and r_{RL} are cross-polarized reflection coefficients; and "L" and "R" respectively represent the LCP and RCP. The absorption rate of the proposed metasurface to the LCP and RCP waves can then be calculated according to the following equations:

$$A_{\mathrm{LCP}} = 1 - |r_{LL}|_2 - |r_{RL}|^2 \tag{3}$$

$$A_{\mathrm{RCP}} = 1 - |r_{RR}|_2 - |r_{LR}|^2 \tag{4}$$

The magnitude of the difference in the SSA effect of the metasurface can be measured by the CD index:

$$CD = A_{\mathrm{LCP}} - A_{\mathrm{RCP}} \tag{5}$$

In order to achieve independent and efficient regulation of terahertz CP waves using the metasurface, the PB phase is introduced to independently regulate CP waves, so that each unit cell on the metasurface has a reflection wave with the same amplitude and an independently adjustable phase. When the unit cell rotates along the z-axis at a degree of φ, then the reflection matrix can be deduced according to the following equation:

$$\boldsymbol{R}_{\mathrm{circ}}(\varphi) = \boldsymbol{M}(-\varphi)\boldsymbol{R}_{\mathrm{circ}}\boldsymbol{M}(\varphi) = \begin{pmatrix} r_{LR} & r_{LL} \cdot e^{-\mathrm{i}2\varphi} \\ r_{RR} \cdot e^{\mathrm{i}2\varphi} & r_{RL} \end{pmatrix} \tag{6}$$

The rotation matrix $\boldsymbol{M}(\varphi) = \begin{pmatrix} \cos\varphi & \sin\varphi \\ -\sin\varphi & \cos\varphi \end{pmatrix}$. Thus, when the rotation angle of the unit cell is φ, an additional phase retardation with $2 * \varphi$ can be introduced in the reflected wave. Therefore, by controlling the change in φ and encoding the reflection phase, it is possible to achieve a variety of efficient wavefront manipulations.

3. Results and Discussion

The 3D full-wave numerical simulation software CST Microwave Studio was used to simulate the metasurface unit cell. The reflection coefficient results in Figure 2a demonstrate that the T-SRR has different reflection characteristics for the LCP and RCP incidences. The strong chiral resonances occur at three different frequency points: r_{LL} possesses the low values of 0.04 and 0.03 at low frequency (1 THz) and high frequency (1.29 THz), respectively, r_{RR} reaches the minimum value of 0.01 at medium frequency (1.17 THz), meanwhile the cross-polarized reflection coefficients r_{LR} and r_{RL} can be efficiently suppressed in the entire frequency band from 0.9 to 1.4 THz. The absorption of the LCP and RCP waves of the T-SRR in Figure 2b is calculated from the reflection coefficients, and the results showed that: A_{LCP} is 98.7% and A_{RCP} is only 18.7% at 1 THz; A_{LCP} is 31.1% and A_{RCP} is only 97.6% at 1.17 THz; and A_{LCP} is 94.4% and A_{RCP} is only 30.0% at 1.29 THz. Therefore, it can be concluded that the T-SRR could achieve strong CD in the three frequency bands, where

the three CD peaks are 0.80 (1 THz), −0.66 (1.17 THz), and 0.64 (1.29 THz), as shown in Figure 2c.

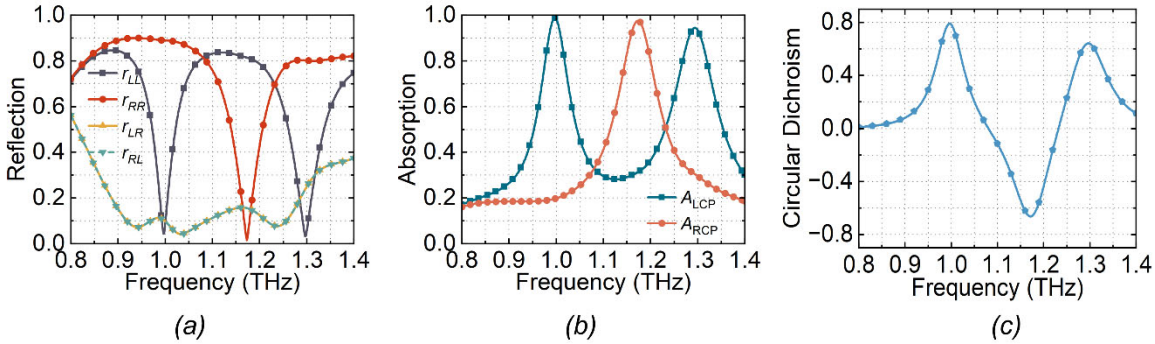

Figure 2. Simulation results of SSA effect of the T-SRR unit cell. (**a**) Reflection coefficient of the T-SRR; (**b**) Absorption of the LCP and RCP waves of the T-SRR; (**c**) Circular dichroism of the T-SRR.

The SSA performance of the proposed T-SRR under different incident angles is also further discussed. The angle between the incident CP waves and the *z*-axis is defined as θ, and Figure 3a,b show the LCP absorption rate and RCP absorption rate of the T-SRR using different values of θ. The absorption spectrum demonstrated that the three chiral resonance frequency points of the T-SRR do not shift with the increase in θ. It can be observed that even if θ increases up to 60°, the T-SRR can still have absorption rates of more than 80% at the three chiral resonance frequency points. Therefore, this metasurface unit cell has excellent angular stability in terms of the SSA effect, which makes it promising tool for complex situations with oblique incidences.

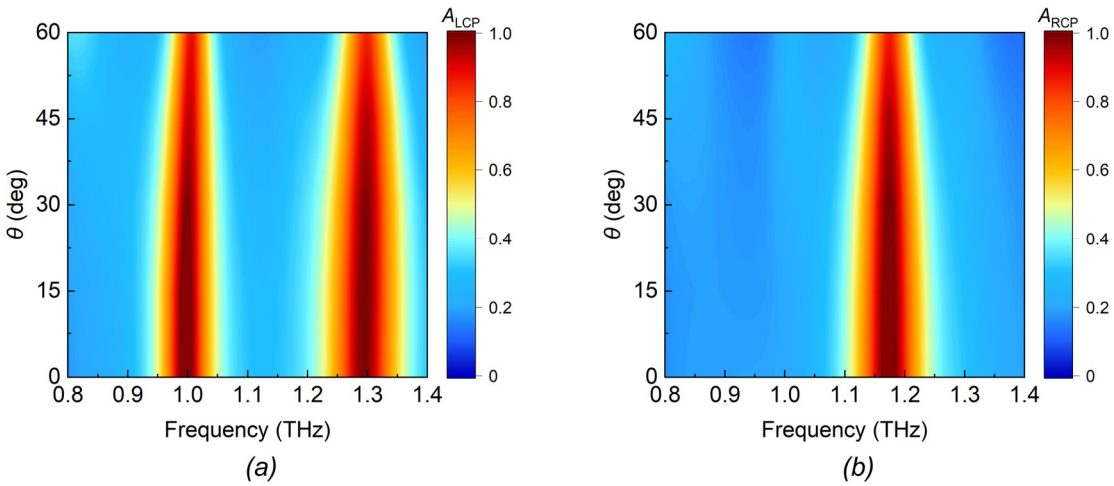

Figure 3. Simulated absorption spectrum of the T-SRR unit cell under different oblique incident angles. (**a**) Absorption of LCP waves; (**b**) Absorption of RCP waves.

For the purpose of further comprehending the working mechanism of the triple-band SSA effect, the simulated surface current distributions of the T-SRR unit cell are plotted in Figure 4. At 1 THz, under the LCP incident wave, a pair of antiparallel currents with similar amplitudes (as indicated by the black dash arrow) was excited on both sides of the outer ring of the T-SRR, as shown in Figure 4a. The antiparallel currents can be viewed as a magnetic dipole with a magnetic moment perpendicular to the metasurface plane, which causes the energy of the incident LCP wave to be bound to the surface of the unit cell and dissipated by the ohmic loss effect of the metal and the absorption effect of the lossy substrate PMDS. However, the surface currents excited by the unit cell under the RCP wave were weaker than that of the LCP wave. Figure 4b shows that under the RCP

incidence, similar antiparallel currents were also excited on the T-SRR at 1.17 THz, but the positions are on the left sides of the outer and inner rings. Figure 4c reveals the surface currents of the T-SRR at 1.29 THz. The LCP wave excited the magnetic dipole mode on the respective right sides of the outer and inner rings of the T-SRR, which also led to the high absorption of the LCP wave, but there was no such phenomenon under the radiation of the RCP wave. According to the above analysis, the T-SRR excites the magnetic dipole modes at three different positions under the incidence of CP waves with different handedness, thereby realizing the triple-band SSA effect.

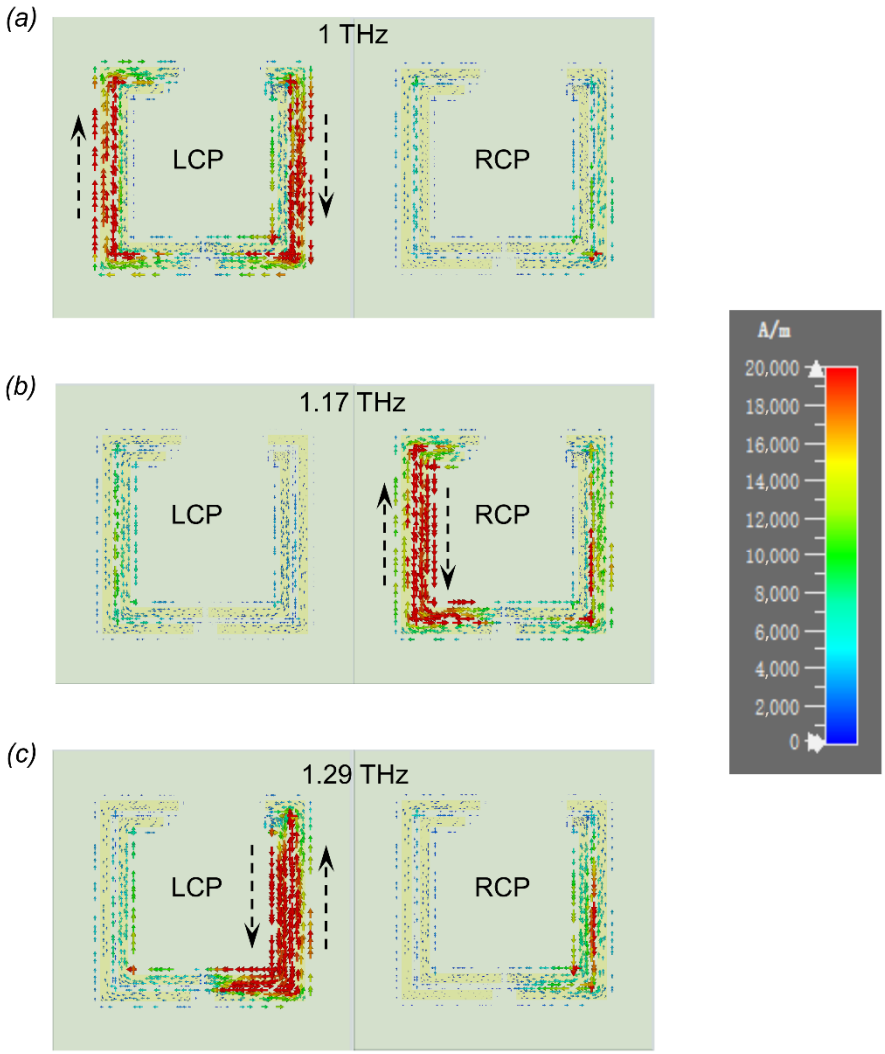

Figure 4. Surface current distributions of the T-SRR under the incidence of CP waves in different spin states. (**a**) T-SRR under the normal incidence of LCP/RCP at 1 THz; (**b**) T-SRR under the normal incidence of LCP/RCP at 1.17 THz; (**c**) T-SRR under the normal incidence of LCP/RCP at 1.29 THz.

According to the theory of Pancharatnam–Berry phase principle, full phase coverage of −180°~180° can be achieved by continuously rotating the metasurface unit cell structure, and this rotation generally does not affect the reflection amplitude. In addition, another remarkable feature of the PB phase is that the phase response of the metasurface unit cell theoretically only depends on the geometric orientation of the unit in a wide bandwidth [32]. Figure 5a shows the schematic of the T-SRR unit cell at a rotation angle of φ, while Figure 5b plots the reflection phase responses of the T-SRR at the three operating frequencies at different rotation angles. Here, only the reflected spin state at the operating frequency needs to be considered. The results show that the phase delay of the T-SRR is nearly linear

with the increase in φ, and the corresponding reflection phase could indeed achieve full coverage of $-180°$~$180°$ as φ increases from 0° to 180°. Interestingly, the phase change of the LCP and RCP waves showed opposing trends. Therefore, it can be inferred that the proposed triple-band SSA chiral metasurface could independently manipulate the CP waves phase at the chiral resonant frequencies.

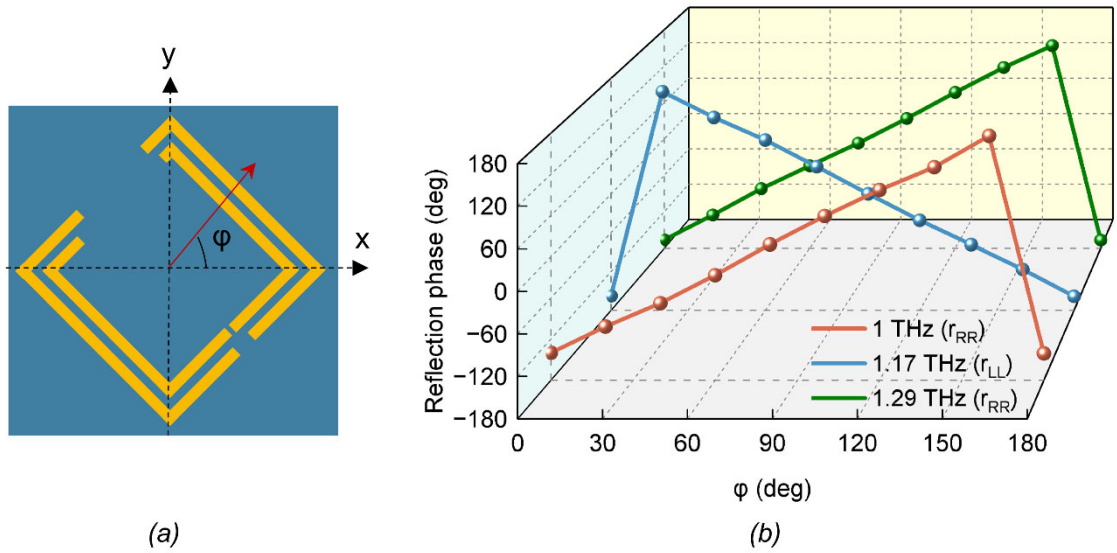

Figure 5. PB phase simulation verification of the T-SRR. (**a**) Schematic of the rotation angle φ of the T-SRR unit cell; (**b**) Reflective phase response of the T-SRR varies with the rotation angle φ at frequency points of 1, 1.17, and 1.29 THz.

To validate that the proposed chiral units have multi-band amplitude and phase manipulation abilities, two types of terahertz-coding metasurface devices were designed and simulated. The first device based on the proposed T-SRR unit cell is a 1-bit coding metasurface, which functions as a four-beam splitter with the SSA effect. As shown in Figure 6a, two units at a rotation angle φ of 0° and 90° are represented by code "0" and code "1", respectively, with a reflection phase difference of 180°. Figure 6b is the schematic diagram of the coding strategy of the 1-bit coding metasurface. Each group of 5 units along the x-axis and y-axis forms a chessboard array. The entire array consists of 30 × 30 units.

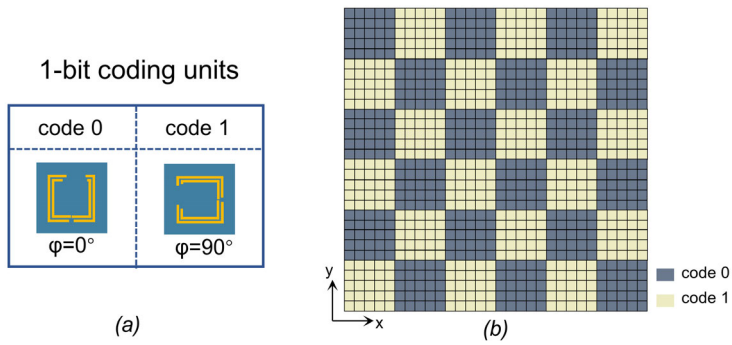

Figure 6. 1-bit coding scheme of the four-beam splitting metasurface. (**a**) Two basic 1-bit coding units; (**b**) Chessboard coding strategy.

Figure 7 shows the far-field scattering patterns of the 1-bit metasurface at 1, 1.17, and 1.29 THz when the LCP and RCP waves impinge on the metasurface along the $-z$-axis. Figure 7a,c show that the LCP waves are absorbed efficiently, and the RCP waves are split into four-directional symmetric beams at 1 and 1.29 THz. Meanwhile, at 1.17 THz, the RCP

wave is highly absorbed and only the LCP wave is split into four-directional symmetric beams, as shown in Figure 7b.

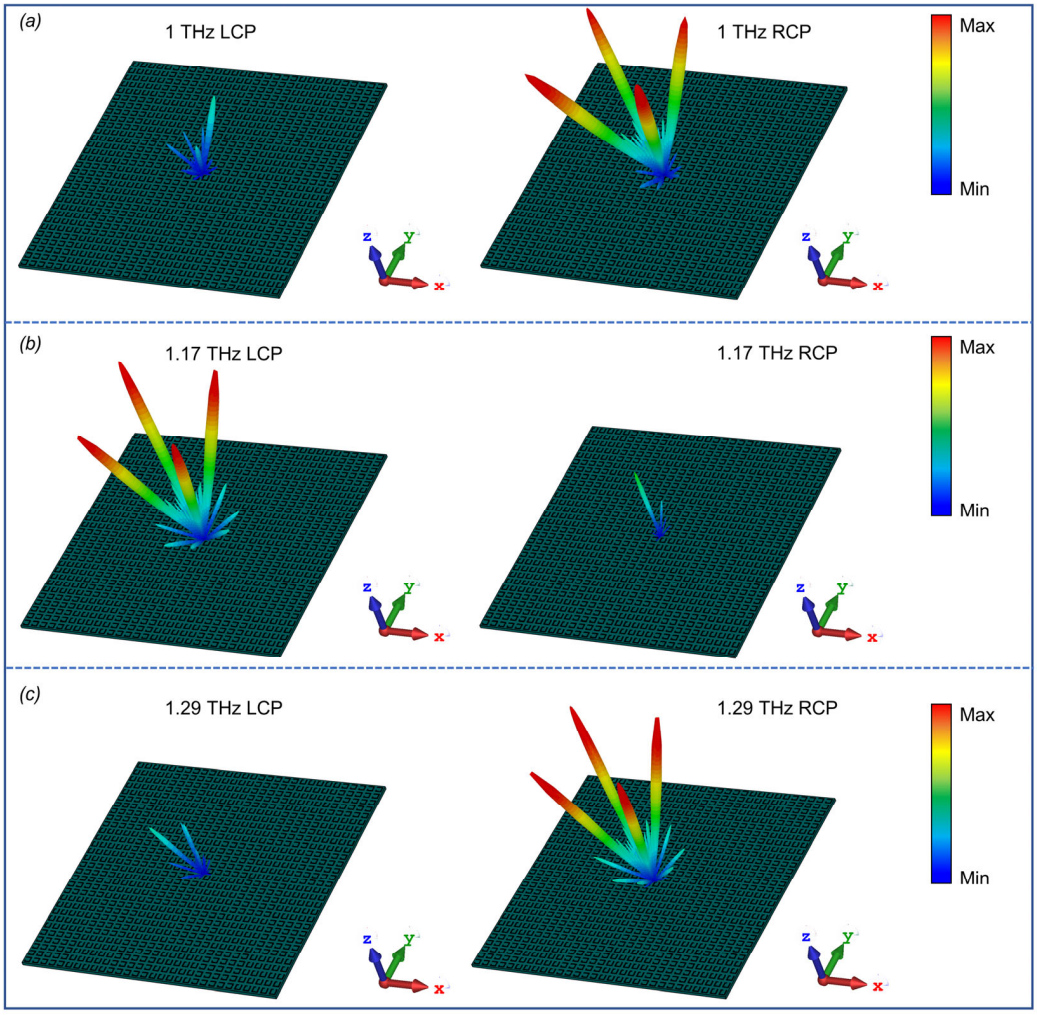

Figure 7. The simulated 3D far-field results for the SSA four-beam splitting metasurface array. (**a**) The array under the normal incidence of LCP/RCP at 1 THz; (**b**) The array under the normal incidence of LCP/RCP at 1.17 THz; (**c**) The array under the normal incidence of LCP/RCP at 1.29 THz.

The second terahertz coding metasurface device is a 2-bit spin-selective vortex beam generator with an anomalous reflection angle. The basic coding units of the metasurface are shown in Figure 8a; four types of the T-SRR units at rotation angles of 22.5°, 67.5°, 112.5°, and 157.5° are represented by codes "0", "1", "2", and "3", respectively, with a reflection phase difference interval of 90°. The orbital angular momentum (OAM) carried by a vortex beam is represented by the phase section of $\exp(il\gamma)$, where γ is the azimuth around the central axis of the beam and l is the topological charge of the vortex mode. A general method for creating the OAM beam is to introduce a spiral-like phase shift via the metasurface, and the phase distribution at each point (x, y) of the metasurface can be calculated as:

$$\gamma(x, y) = l \cdot \arctan\frac{y}{x} \tag{7}$$

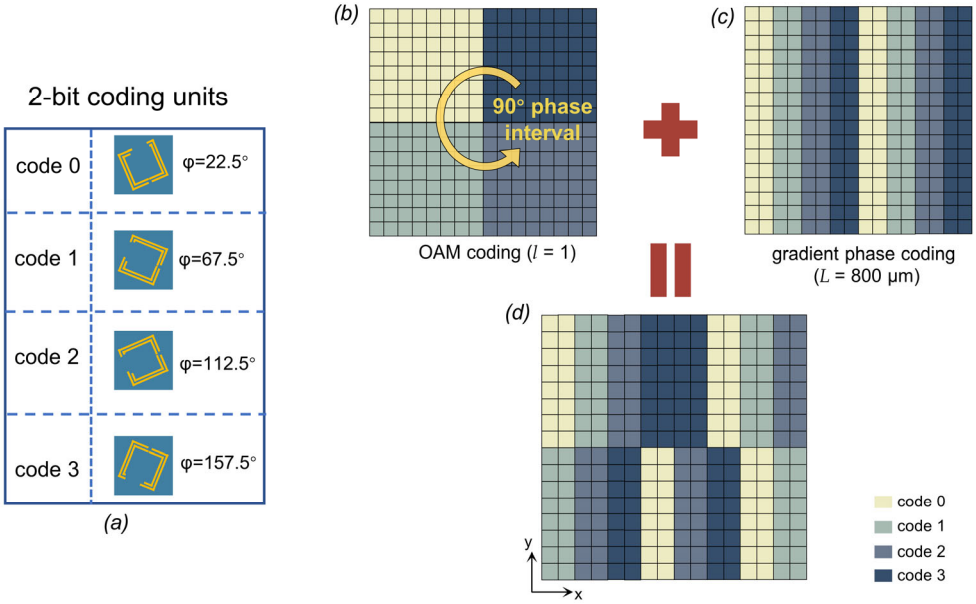

Figure 8. 2-bit coding scheme of the spin-selective vortex beam generator with an anomalous reflection angle. (**a**) Four basic 2-bit coding units; (**b**) Coding strategy with OAM mode l = 1; (**c**) Coding strategy with gradient coding sequence "00112233⋯" varying along the x direction and the physical length of the phase gradient L = 800 μm; (**d**) The mixed coding strategy based on phase superposition of b and c.

The pattern of the OAM coding strategy in Figure 8b generated a vortex beam with OAM mode $l = 1$. Specifically, in order to introduce a spiral-like phase shift, the entire array consists of four sectors with a phase interval of 90° counterclockwise. Figure 8c is a gradient phase encoding strategy along the x-axis, which enables anomalous reflection of the beam. The deflection angle can be determined by the generalized Snell's law:

$$\theta_r = \pm \sin^{-1}(\lambda / L) \tag{8}$$

where λ and L represent the wavelength of the electromagnetic wave in vacuum and the physical length of the supercell constituting the phase gradient, respectively. The CP waves can be flexibly controlled by the digital convolution operation on the scattering patterns of PB-coding metasurface [39]. In this work, the gradient phase coding sequence was superimposed on the OAM coding sequence, as shown in Figure 8d, to achieve anomalous reflection of the vortex beam. The entire array consisted of 16 × 16 units.

Figure 9a–c show the 3D far-field scattering patterns and normalized 2D scattering patterns of the 2-bit metasurface at 1, 1.17, and 1.29 THz under the LCP and RCP incidences along the $-z$-axis, respectively. At 1 THz, the LCP wave was absorbed efficiently, and only the RCP wave was converted to the vortex beam with a −22° deflection angle, as shown in Figure 9a. Simulation results showed that at the center of the reflected beam is a cavity, which is consistent with the characteristic profile of the doughnut-shaped vortex beam. In contrast, at 1.17 THz, the RCP wave was effectively absorbed and the LCP wave was reflected as a vortex beam with a 20° deflection angle, as shown in Figure 9b. Moreover, at 1.29 THz, the LCP wave was highly absorbed while the RCP wave was converted into the vortex beam with a −18° deflection angle, as shown in Figure 9c. Each deflection angle is consistent with the theoretical value calculated from Equation (8).

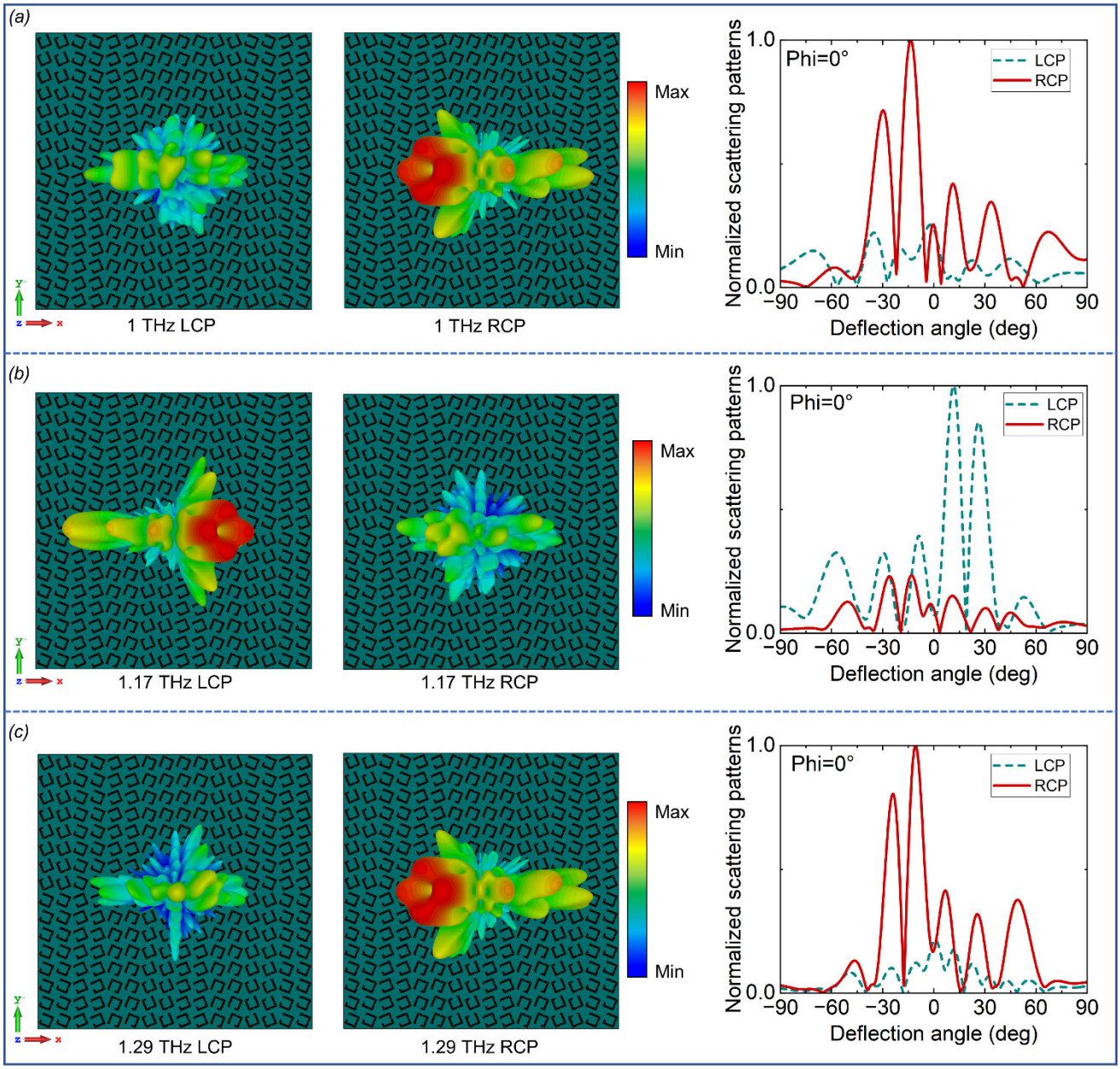

Figure 9. Simulation of the 3D far-field scattering patterns and normalized 2D scattering patterns of the 2-bit metasurface array at the azimuth angle phi = 0°. (**a**) The array under the normal incidence of LCP/RCP at 1 THz; (**b**) The array under the normal incidence of LCP/RCP at 1.17 THz; (**c**) The array under the normal incidence of LCP/RCP at 1.29 THz.

Table 2 provides a comparison between our work and recently reported SSA effect chiral metasurfaces. The majority of the SSA chiral metasurfaces with giant CD usually work at a single frequency band. Compared with some dual-band SSA chiral metasurfaces, our work not only expands the SSA effect frequency band to three, but also maintains a strong CD (>0.5) in all three frequency bands. Furthermore, most of these works do not mention the phase manipulation capability of SSA chiral metasurfaces because the pattern designs of these metasurfaces do not support the introduction of a PB phase.

Table 2. Comparison of our work with previously reported reflective metasurfaces with CD properties.

Ref.	Spectrum	Band Coverage	*CD* Peaks	Phase Manipulation
[30]	Terahertz	Single band	0.87	Not mentioned
[33]	Microwave	Single band	0.85	Yes
[35]	Microwave	Dual bands	0.78 (1st band) 0.69 (2nd band)	Not mentioned
[38]	Microwave	Dual bands	0.72 (1st band) −0.79 (2nd band)	Not mentioned
[36]	Mid-infrared	Dual bands	<0.6	Not mentioned
[29]	Terahertz	Dual bands	0.64 (1st band) 0.75 (2nd band)	Yes
This work	Terahertz	Triple bands	0.80 (1st band) −0.66 (2nd band) 0.64 (3rd band)	Yes

4. Conclusions

In summary, we have proposed a design method to extend the SSA effect bands of chiral metasurfaces in the terahertz region, and successfully extended the strong CD of chiral metasurfaces to three frequency bands. The simulated CD results showed that the metasurface unit cell has three peaks of 0.80, −0.66, and 0.64 at 1, 1.17, and 1.29 THz, respectively. In addition, the introduction of the PB phase enabled the metasurface unit cell to independently manipulate the reflection phase in the three frequency bands. To illustrate that this metasurface can achieve simultaneous manipulation of amplitude and phase according to the circular polarization direction of incident electromagnetic waves, two kinds of metasurface-based terahertz spin-selective devices were simulated and studied, both exhibiting good SSA effect and efficient wavefront manipulation. Furthermore, due to the scalability of Maxwell's equations, our scheme can be further applied to other frequencies, indicating that it also has potential applications in photonics, such as spectroscopy and sensing.

Author Contributions: Conceptualization, L.S.; methodology, L.S., J.D. and H.Z.; theories, H.Z., L.S. and J.D.; simulation analysis, H.Z., T.M., L.D. and R.N.; validation and data analysis, H.Z., T.M., L.D., R.N., X.B. and H.S.; writing—original draft preparation, L.S., H.Z. and J.D.; writing—review and editing, L.S., H.Z. and J.D.; supervision, L.S. and J.D. All authors have read and agreed to the published version of the manuscript.

Funding: This research was funded by the National Key R&D Program of China (Grant No. 2022YFF0604801), the National Natural Science Foundation of China (Grant Nos. 62271056, 62171186, 62201037, and 61527805), the Beijing Natural Science Foundation of China-Haidian Original Innovation Joint Fund (Grant No. L222042), the Beijing Natural Science Foundation (Grant No. 4154085), the Open Research Fund of State Key Laboratory of Space-Ground Integrated Information Technology (Grant No. 6142221200201), the Basic Research Foundation of Beijing Institute of Technology, China (Grant No. BITBLR2020014), and the 111 Project of China (Grant No. B14010).

Conflicts of Interest: The authors declare no conflict of interest.

References

1. Shen, S.; Liu, X.; Shen, Y.; Qu, J.; Pickwell-MacPherson, E.; Wei, X.; Sun, Y. Recent Advances in the Development of Materials for Terahertz Metamaterial Sensing. *Adv. Opt. Mater.* **2022**, *10*, 2101008. [CrossRef]
2. Kleiner, R. Filling the Terahertz Gap. *Science* **2007**, *318*, 1254–1255. [CrossRef] [PubMed]
3. Yu, N.; Capasso, F. Flat Optics with Designer Metasurfaces. *Nat. Mater.* **2014**, *13*, 139–150. [CrossRef] [PubMed]
4. Dong, L.; Si, L.; Xu, H.; Shen, Q.; Lv, X.; Zhuang, Y.; Zhang, Q. Rapid Customized Design of a Conformal Optical Transparent Metamaterial Absorber Based on the Circuit Analog Optimization Method. *Opt. Express* **2022**, *30*, 8303–8316. [CrossRef]
5. Fan, K.; Suen, J.Y.; Liu, X.; Padilla, W.J. All-Dielectric Metasurface Absorbers for Uncooled Terahertz Imaging. *Optica* **2017**, *4*, 601–604. [CrossRef]
6. Chen, X.; Huang, L.; Mühlenbernd, H.; Li, G.; Bai, B.; Tan, Q.; Jin, G.; Qiu, C.-W.; Zhang, S.; Zentgraf, T. Dual-Polarity Plasmonic Metalens for Visible Light. *Nat. Commun.* **2012**, *3*, 1198. [CrossRef]

7. Zhao, F.; Li, Z.; Dai, X.; Liao, X.; Li, S.; Cao, J.; Shang, Z.; Zhang, Z.; Liang, G.; Chen, G.; et al. Broadband Achromatic Sub-Diffraction Focusing by an Amplitude-Modulated Terahertz Metalens. *Adv. Opt. Mater.* **2020**, *8*, 2000842. [CrossRef]
8. Fang, S.; Luan, K.; Ma, H.F.; Lv, W.; Li, Y.; Zhu, Z.; Guan, C.; Shi, J.; Cui, T.J. Asymmetric Transmission of Linearly Polarized Waves in Terahertz Chiral Metamaterials. *J. Appl. Phys.* **2017**, *121*, 033103. [CrossRef]
9. Stolarek, M.; Yavorskiy, D.; Kotyński, R.; Rodríguez, C.J.Z.; Łusakowski, J.; Szoplik, T. Asymmetric Transmission of Terahertz Radiation through a Double Grating. *Opt. Lett.* **2013**, *38*, 839–841. [CrossRef]
10. Zhang, H.; Yang, C.; Liu, M.; Zhang, Y. Dual-Function Tuneable Asymmetric Transmission and Polarization Converter in Terahertz Region. *Results Phys.* **2021**, *25*, 104242. [CrossRef]
11. Cheng, G.; Si, L.; Tang, P.; Zhang, Q.; Lv, X. Study of Symmetries of Chiral Metasurfaces for Azimuth-Rotation-Independent Cross Polarization Conversion. *Opt. Express* **2022**, *30*, 5722–5730. [CrossRef] [PubMed]
12. Cheng, G.; Si, L.; Tang, P.; Zhuang, Y.; Sun, H.; Ding, J. Topology Optimization of the Azimuth-Rotation-Independent Polarization Conversion Metasurface for Bandwidth Enhancement. *Opt. Express* **2022**, *30*, 41340–41349. [CrossRef] [PubMed]
13. Yang, Q.; Wang, Y.; Liang, L.; Yang, M. Broadband Transparent Terahertz Vortex Beam Generator Based on Thermally Tunable Geometric Metasurface. *Opt. Mater.* **2021**, *121*, 111574. [CrossRef]
14. Yue, Z.; Liu, J.; Li, J.; Li, J.; Zheng, C.; Wang, G.; Chen, M.; Xu, H.; Wang, Q.; Xing, X.; et al. Multifunctional Terahertz Metasurfaces for Polarization Transformation and Wavefront Manipulation. *Nanoscale* **2021**, *13*, 14490–14496. [CrossRef] [PubMed]
15. Liang, Y.; Lin, H.; Koshelev, K.; Zhang, F.; Yang, Y.; Wu, J.; Kivshar, Y.; Jia, B. Full-Stokes Polarization Perfect Absorption with Diatomic Metasurfaces. *Nano Lett.* **2021**, *21*, 1090–1095. [CrossRef]
16. Liang, Y.; Koshelev, K.; Zhang, F.; Lin, H.; Lin, S.; Wu, J.; Jia, B.; Kivshar, Y. Bound States in the Continuum in Anisotropic Plasmonic Metasurfaces. *Nano Lett.* **2020**, *20*, 6351–6356. [CrossRef]
17. Ahmadivand, A.; Gerislioglu, B.; Ahuja, R.; Kumar Mishra, Y. Terahertz Plasmonics: The Rise of Toroidal Metadevices towards Immunobiosensings. *Mater. Today* **2020**, *32*, 108–130. [CrossRef]
18. Eidelshtein, G.; Fardian-Melamed, N.; Gutkin, V.; Basmanov, D.; Klinov, D.; Rotem, D.; Levi-Kalisman, Y.; Porath, D.; Kotlyar, A. Synthesis and Properties of Novel Silver-Containing DNA Molecules. *Adv. Mater.* **2016**, *28*, 4839–4844. [CrossRef]
19. Plum, E.; Zheludev, N.I. Chiral Mirrors. *Appl. Phys. Lett.* **2015**, *106*, 221901. [CrossRef]
20. Wang, Q.; Plum, E.; Yang, Q.; Zhang, X.; Xu, Q.; Xu, Y.; Han, J.; Zhang, W. Reflective Chiral Meta-Holography: Multiplexing Holograms for Circularly Polarized Waves. *Light Sci. Appl.* **2018**, *7*, 25. [CrossRef]
21. Basiri, A.; Chen, X.; Bai, J.; Amrollahi, P.; Carpenter, J.; Holman, Z.; Wang, C.; Yao, Y. Nature-Inspired Chiral Metasurfaces for Circular Polarization Detection and Full-Stokes Polarimetric Measurements. *Light Sci. Appl.* **2019**, *8*, 78. [CrossRef] [PubMed]
22. Hajji, M.; Cariello, M.; Gilroy, C.; Kartau, M.; Syme, C.D.; Karimullah, A.; Gadegaard, N.; Malfait, A.; Woisel, P.; Cooke, G.; et al. Chiral Quantum Metamaterial for Hypersensitive Biomolecule Detection. *ACS Nano* **2021**, *15*, 19905–19916. [CrossRef] [PubMed]
23. Wang, Z.; Jia, H.; Yao, K.; Cai, W.; Chen, H.; Liu, Y. Circular Dichroism Metamirrors with Near-Perfect Extinction. *ACS Photonics* **2016**, *3*, 2096–2101. [CrossRef]
24. Jing, L.; Wang, Z.; Yang, Y.; Zheng, B.; Liu, Y.; Chen, H. Chiral Metamirrors for Broadband Spin-Selective Absorption. *Appl. Phys. Lett.* **2017**, *110*, 231103. [CrossRef]
25. Stojanovic, D.B.; Gligoric, G.; Belicev, P.P.; Belic, M.R.; Hadzievski, L. Circular Polarization Selective Metamaterial Absorber in Terahertz Frequency Range. *IEEE J. Sel. Top. Quantum Electron.* **2021**, *27*, 1–6. [CrossRef]
26. Ouyang, L.; Rosenmann, D.; Czaplewski, D.A.; Gao, J.; Yang, X. Broadband Infrared Circular Dichroism in Chiral Metasurface Absorbers. *Nanotechnology* **2020**, *31*, 295203. [CrossRef]
27. Liu, M.; Plum, E.; Li, H.; Duan, S.; Li, S.; Xu, Q.; Zhang, X.; Zhang, C.; Zou, C.; Jin, B.; et al. Switchable Chiral Mirrors. *Adv. Opt. Mater.* **2020**, *8*, 2000247. [CrossRef]
28. Zhang, Y.; Liu, H.; Xu, R.; Qin, Z.; Teng, C.; Deng, S.; Chen, M.; Cheng, Y.; Deng, H.; Yang, H.; et al. Tunable Circular Dichroism Based on Graphene-Metal Split Ring Resonators. *Opt. Express* **2021**, *29*, 21020–21030. [CrossRef]
29. Li, H.; Li, J.; Zheng, C.; Xu, H.; Yang, F.; Li, J.; Li, J.; Yue, Z.; Shi, W.; Shi, W.; et al. Dual-Band Giant Spin-Selective Full-Dimensional Manipulation of Graphene-Based Chiral Meta-Mirrors for Terahertz Waves. *Opt. Express* **2022**, *30*, 22292–22305. [CrossRef]
30. Cui, Y.; Wang, X.; Jiang, H.; Jiang, Y. High-Efficiency and Tunable Circular Dichroism in Chiral Graphene Metasurface. *J. Phys. Appl. Phys.* **2022**, *55*, 135102. [CrossRef]
31. Wang, H.; Jing, Y.; Li, Y.; Huang, L.; Feng, M.; Yuan, Q.; Wang, J.; Zhang, J.; Qu, S. Spin-Selective Corner Reflector for Retro-Reflection and Absorption by a Circular Dichroitic Manner. *Photonics Res.* **2021**, *9*, 726. [CrossRef]
32. Jing, L.; Wang, Z.; Maturi, R.; Zheng, B.; Wang, H.; Yang, Y.; Shen, L.; Hao, R.; Yin, W.; Li, E.; et al. Gradient Chiral Metamirrors for Spin-Selective Anomalous Reflection. *Laser Photonics Rev.* **2017**, *11*, 1700115. [CrossRef]
33. Lin, M.; Liu, C.; Yi, J.; Jiang, Z.H.; Chen, X.; Xu, H.-X.; Burokur, S.N. Chirality-Intrigged Spin-Selective Metasurface and Applications in Generating Orbital Angular Momentum. *IEEE Trans. Antennas Propag.* **2022**, *70*, 4549–4557. [CrossRef]
34. Huang, Y.; Xiao, T.; Xie, Z.; Zheng, J.; Su, Y.; Chen, W.; Liu, K.; Tang, M.; Müller-Buschbaum, P.; Li, L. Single-Layered Reflective Metasurface Achieving Simultaneous Spin-Selective Perfect Absorption and Efficient Wavefront Manipulation. *Adv. Opt. Mater.* **2021**, *9*, 2001663. [CrossRef]
35. Wang, L.; Huang, X.; Li, M.; Dong, J. Chirality Selective Metamaterial Absorber with Dual Bands. *Opt. Express* **2019**, *27*, 25983–25993. [CrossRef]

36. Tang, H.; Rosenmann, D.; Czaplewski, D.A.; Yang, X.; Yang, X.; Gao, J.; Gao, J.; Gao, J. Dual-Band Selective Circular Dichroism in Mid-Infrared Chiral Metasurfaces. *Opt. Express* **2022**, *30*, 20063–20075. [CrossRef]
37. Gou, Y.; Ma, H.F.; Wang, Z.X.; Wu, L.W.; Wu, R.Y.; Cui, T.J. Dual-Band Chiral Metasurface for Independent Controls of Spin-Selective Reflections. *Opt. Express* **2022**, *30*, 12775–12787. [CrossRef]
38. Gao, W.; Huang, C.; Feng, Z.; Li, M.; Dong, J. Circular Dichroism Metamirror with Diversified Chiral Molecules Combinations. *Opt. Express* **2021**, *29*, 33367–33379. [CrossRef]
39. Zhang, L.; Liu, S.; Li, L.; Cui, T.J. Spin-Controlled Multiple Pencil Beams and Vortex Beams with Different Polarizations Generated by Pancharatnam-Berry Coding Metasurfaces. *ACS Appl. Mater. Interfaces* **2017**, *9*, 36447–36455. [CrossRef]